

# Role of Si in Improving the Shape Recovery of FeMnSiCrNi Shape Memory Alloys

BIKAS C. MAJI, MADANGOPAL KRISHNAN, GOUTHAMA, and R.K. RAY

The effect of Si addition on the microstructure and shape recovery of FeMnSiCrNi shape memory alloys has been studied. The microstructural observations revealed that in these alloys the microstructure remains single-phase austenite ( $\gamma$ ) up to 6 pct Si and, beyond that, becomes two-phase  $\gamma + \delta$  ferrite. The  $\text{Fe}_5\text{Ni}_3\text{Si}_2$  type intermetallic phase starts appearing in the microstructure after 7 pct Si and makes these alloys brittle. Silicon addition does not affect the transformation temperature and mechanical properties of the  $\gamma$  phase until 6 pct, though the amount of shape recovery is observed to increase monotonically. Alloys having more than 6 pct Si show poor recovery due to the formation of  $\delta$ -ferrite. The shape memory effect (SME) in these alloys is essentially due to the  $\gamma$  to stress-induced  $\varepsilon$  martensite transformation, and the extent of recovery is proportional to the amount of stress-induced  $\varepsilon$  martensite. Alloys containing less than 4 pct and more than 6 pct Si exhibit poor recovery due to the formation of stress-induced  $\alpha'$  martensite through  $\gamma$ - $\varepsilon$ - $\alpha'$  transformation and the large volume fraction of  $\delta$ -ferrite, respectively. Silicon addition decreases the stacking fault energy (SFE) and the shear modulus of these alloys and results in easy nucleation of stress-induced  $\varepsilon$  martensite; consequently, the amount of shape recovery is enhanced. The amount of athermal  $\varepsilon$  martensite formed during cooling is also observed to decrease with the increase in Si.

DOI: 10.1007/s11661-011-0651-x

© The Minerals, Metals & Materials Society and ASM International 2011

## I. INTRODUCTION

THE shape memory effect (SME) associated with the  $\gamma$  (fcc)- $\varepsilon$  (hcp) martensite transformation was first demonstrated by Enami *et al.*<sup>[1]</sup> in a polycrystalline Fe-18.5 pct Mn alloy, although the amount of shape recovery was very small (<10 pct). Subsequently, Sato *et al.*<sup>[2]</sup> reported that the addition of 1 pct Si in Fe-30Mn single crystal can improve the shape recovery to a great extent by enhancing the formation of  $\varepsilon$  martensite. A little later Murakami *et al.*<sup>[3]</sup> successfully developed the polycrystalline Fe-Mn-Si alloys, which show more than 1.7 pct recovery strain. These researchers also showed that in Fe-Mn-Si alloys containing 32 pct of Mn, the extent of shape recovery increases with Si content up to 6.5 pct. These Fe-Mn-Si based shape memory alloys have been studied for a long time because of their lower cost, good workability, excellent machinability, and weldability. However, one of the major limitations with these alloys is the amount of fully reversible strain. Normally, in these alloys, the available fully recoverable strain is only 2 pct, beyond which the recovery is incomplete. Although, according to the shear model for the fcc-hcp martensitic transformation where hcp

$\varepsilon$  martensite can be formed by shearing along  $\langle 112 \rangle_\gamma$  on every alternate  $\{111\}_\gamma$  plane of the fcc  $\gamma$  phase, at least 17 pct reversible strain should be potentially available. This incomplete recovery is mainly due to the plastic deformation of the  $\gamma$  matrix and formation of strain-induced  $\alpha'$  martensite at the intersecting junctions of  $\varepsilon$  martensite variants. Another limitation that restricts the practical use of these alloys is the corrosion resistance. However, Otsuka *et al.*<sup>[4]</sup> added Cr and Ni to these ternary Fe-Mn-Si alloys to improve the corrosion resistance property and developed corrosion-resistant Fe-Mn-Si-Cr-Ni alloys.

Many researchers have tried to improve the shape recovery of these alloys by different approaches. One of the simplest approaches is to enhance the strength of the  $\gamma$  matrix, which will reduce the amount of plastic deformation while prestraining. The matrix strength can be enhanced directly either by solid solution strengthening or by precipitation hardening with introducing coherent precipitates.<sup>[5,6]</sup> Suitable thermomechanical treatment (like training), which will decrease the stress requirement for stress inducing  $\varepsilon$  martensite, can also effectively improve the recovery by reducing the irrecoverable plastic deformation within the  $\gamma$  matrix.<sup>[7]</sup> On the other hand, some other researchers have tried to improve upon the second cause of incomplete recovery, *i.e.*, to restrict the formation of strain-induced  $\alpha'$  martensite, which is believed to hinder the motion of the Shockley partial dislocations during reverse transformation. This could be easily achieved by stress inducing single variant  $\varepsilon$  martensite so that the formation of strain-induced  $\alpha'$  martensite does not take place.<sup>[8]</sup>

BIKAS C. MAJI and MADANGOPAL KRISHNAN, Scientific Officers, are with the Materials Science Division, Bhabha Atomic Research Centre, Mumbai 400 085, India. Contact e-mail: bikchan@barc.gov.in GOUTHAMA, Associate Professor, is with the Department of Materials Science and Engineering, Indian Institute of Technology, Kanpur 208 016, India. R.K. RAY, Visiting Scientist, is with the R and D Division, Tata Steel, Jamshedpur 831 007, India.

Manuscript submitted July 5, 2010.

Article published online March 22, 2011

Based on different avenues available for improving shape recovery, it seems that suitable alloying addition is very important in order to achieve good shape recovery. Silicon is one such element that has been unanimously reported to improve the shape memory in these alloys. According to Sato *et al.*<sup>[9]</sup> and Murakami *et al.*,<sup>[10]</sup> the beneficial effect of Si addition toward shape recovery of Fe-Mn-Si alloys can be attributed to three major factors: (1) lowering of the paramagnetic to antiferromagnetic Neel transformation temperature ( $T_N$ ) of the  $\gamma$  phase below the  $\gamma$  to  $\varepsilon$  martensite start transformation temperature ( $M_S$ ) without disturbing the  $M_S$  temperature; (2) improvement of the strength of the  $\gamma$  matrix; and (3) lowering of the stacking fault energy (SFE) of the  $\gamma$  phase. Murakami *et al.*<sup>[10]</sup> also claimed that the relative position of the  $M_S$  and  $T_N$  temperatures is of outmost importance, because the stress-induced transformation will not take place if  $T_N$  lies above  $M_S$  and no shape recovery can be achieved. On the other hand, Andersson *et al.*<sup>[11]</sup> showed that it is possible to form a large amount of  $\varepsilon$  martensite even when the  $\gamma$  has undergone antiferromagnetic transition, as in the case of  $M_S < T_N$ . Gulyaev<sup>[12]</sup> reported that the addition of Si significantly enhances the yield strength (YS) from 180 MPa for Fe-30Mn to 350 MPa for Fe-30Mn-5.5Si. It is also well known that Si lowers the SFE of the  $\gamma$  phase,<sup>[13]</sup> which favors the formation of  $\varepsilon$  martensite. Tsuzaki *et al.*<sup>[14]</sup> and Tomota *et al.*<sup>[15]</sup> studied the effect of thermal cycling between  $M_f$  and  $A_f$  in Fe-15.5Mn, Fe-24.4Mn, Fe-15.5Mn-6Si, and Fe-24.5Mn-6Si (all in mass pct) alloys and contend that Si causes the improvement in shape recovery by making the movement of partial dislocations reversible and restricting permanent slip in the  $\gamma$  phase. In another study, Gavriljuk *et al.*<sup>[16]</sup> reported that Si increases the concentration of free electrons, which promotes the tendency for short-range ordering and assists in improvement of shape recovery.

These studies show that Si addition is indispensable in achieving a good SME in Fe-Mn-Si based alloys. However, in most of the Fe-Mn-Si-Cr-Ni based alloys, where the  $T_N$  temperature lies well below the  $M_S$  temperature due to the presence of Cr and lower amounts of Mn,<sup>[17]</sup> the exact role played by Si in improving the shape recovery is not clearly understood. Though the amount of Si in these alloys is usually maintained at  $\sim$  (5 to 6) pct, the minimum amount of Si that is actually required to achieve the maximum shape recovery is not known. In the present study, we have made an attempt to determine the exact role of Si in the shape recovery of Fe-Mn-Si-Cr-Ni based shape memory alloys, by studying their microstructure, transformation temperature, mechanical properties, and shape recovery.

## II. EXPERIMENTAL

The nominal compositions of the alloys used in the present work are given in Table I. Alloy buttons were prepared by nonconsumable vacuum arc melting under argon atmosphere using high-purity (99.95 pct) Fe, Mn, Ni, Cr, and Si. These arc-melted buttons were hot rolled

**Table I. Nominal Alloy Compositions**

Alloy	Nominal Composition (Mass Pct)				
	Mn	Cr	Ni	Si	Fe
1	14	9	5	1	balance
2	14	9	5	2	balance
3	14	9	5	3	balance
4	14	9	5	4	balance
5	14	9	5	5	balance
6	14	9	5	6	balance
7	14	9	5	7	balance
8	14	9	5	8	balance
10	14	9	5	10	balance

at 1198 K (925 °C) into strips of 0.5-mm thickness, which were further solution heat treated and used for microstructural and shape memory property evaluation. The specimens were sealed in quartz capsules and solution heat treatment was carried out at 1273 K (1000 °C) for 1 hour. At the end of the heat treatment, these specimens were directly quenched into a water bath by breaking the quartz capsules.

Optical microscopy, X-ray diffraction (XRD), and scanning electron microscopy (SEM) were employed for microstructural characterization. XRD analysis was carried out using Mo  $K_\alpha$  radiation ( $\lambda_{K\alpha 1} = 0.07093$  nm,  $\lambda_{K\alpha 2} = 0.071359$  nm). The chemical compositions of these phases were established using electron probe microanalysis (EPMA). The forward and reverse martensite transformation temperatures were determined on a differential scanning calorimeter (DSC) at a heating/cooling rate of 10 K/min. The shape recovery of these alloys was evaluated using simple bend test. A schematic diagram of the bend test used for measuring the amount of shape recovery is shown in Figure 6(a). The amount of recovery was determined by applying a prestrain between 2 to 8 pct at room temperature followed by a recovery annealing at 873 K (600 °C) temperature for 10 minutes. The amount of prestrain was estimated by using the relationship  $\varepsilon_p = t/d$  and implemented by selecting an appropriate mandrel diameter ( $d$ ). The percentage recovery was calculated on the basis of change in angular distance of the prestrained specimens before and after recovery annealing using the following relationship:

$$\text{Recovery(pct)} = \{(180 - \theta_e - \theta_r)/(180 - \theta_e)\} \times 100 \quad [1]$$

Room-temperature tensile tests were performed at a strain rate of  $6.7 \times 10^{-4}$  in an electromechanical tensile testing machine using tensile specimens of 12.5-mm gage length.

## III. RESULTS

### A. Hot Rollability

Hot rolling experiments were conducted at 1198 K (925 °C) using arc-melted buttons of alloys mentioned

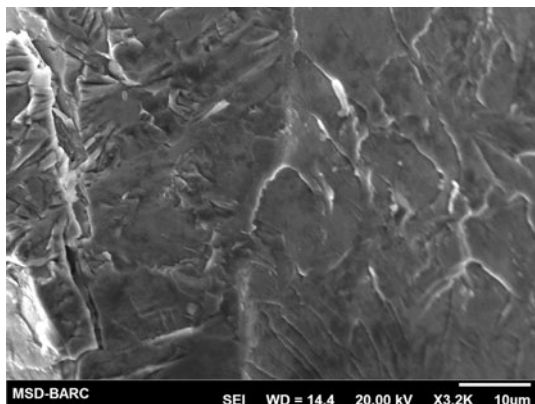


Fig. 1—Scanning electron micrograph taken from the fracture surface of alloy 8 after hot rolling at 1198 K (925 °C).

in Table I. These rolling experiments revealed that with increasing Si these alloys lose their hot deformability. Alloys containing more than 7 pct Si (alloy 8 and alloy 10) are brittle and could not be hot rolled at this temperature. The SEM observation of the fracture surface of alloy 8, as shown in Figure 1, reveals that this alloy shows a typical cleavage type brittle fracture. The brittleness in these alloys is probably associated with the formation of brittle intermetallic (silicide) phase due to higher amounts of Si, a detailed analysis of which will be shown in Section III-B.

### B. Microstructure

Figure 2 shows the optical micrographs taken from alloys 1 through 10 after solution heat treatment. In most of the alloys, the metallographic observations were carried out on hot-rolled and 1273 K (1000 °C) for 1 hour solutionized specimens. However, in the case of alloys 8 and 10, specimens were directly cut from the arc-melted buttons and solution heat treated at 1273 K (1000 °C) for 6 hours, because these alloys could not be hot rolled into strips. Figures 2(a) through (e) show the optical micrographs taken from alloys with 1 to 6 pct Si (alloys 1 through 6). The microstructure of these alloys is essentially composed of single-phase  $\gamma$ , which transforms to  $\varepsilon$  martensite while water quenching. A closer look into these micrographs also reveals that the amount of martensite decreases with increasing Si amount. Alloy containing 7 pct Si shows a two-phase microstructure (Figure 2(f)) consisting of the  $\gamma$  (the matrix phase) and another blocky phase (the darker phase), which is possibly  $\delta$ -ferrite. The amount of this second phase in this alloy was measured by area fraction and found to be ~45 pct. The microstructures of alloys containing more than 7 pct Si consist of multiple phases. The microstructure of alloy 8 (Figure 2(g)) clearly reveals the presence of three phases. Apart from the matrix phase, one phase appears as elongated plates along the grain boundaries and inside the grains. This phase is possibly an intermetallic phase and may be the reason for the brittleness in these alloys. Besides this intermetallic phase, another phase could also be noticed

in this sample, which appears as large grains (bright in contrast) adjacent to the grain boundaries. A further increase in the Si amount to 10 pct results in an increased amount of intermetallic phase, and the large bright grains adjacent to the boundaries (observed in Figure 2(g)) are totally absent. The metallograph obtained from alloy 10 shown in Figure 2(h) also reveals another interesting feature: unlike the matrix of alloy 8 in this alloy, some equiaxed grains are clearly visible within the matrix. The possible reason behind this will be illustrated in Section IV.

The XRD patterns obtained from alloys 1 through 7 after solutionizing, as shown in Figure 3(a), clearly reveal that alloys with up to 6 pct Si show reflections that could be readily indexed to  $\gamma$  and  $\varepsilon$  martensite phases. However, the diffractogram taken from alloy 7 contains some extra reflections apart from the reflections of these two phases. The  $2\theta$  positions of these reflections match exactly with the positions of  $\delta$ -ferrite having a lattice parameter of 0.2859 nm. Therefore, the blocky dark phase shown in the optical microstructure taken from alloy 7 is  $\delta$ -ferrite (Figure 2(f)), which appears due to a higher amount of Si addition, because Si is known to be a strong ferrite stabilizer.<sup>[18]</sup> The XRD pattern obtained from alloy 8 (Figure 3(b)) shows the presence of many extra reflections apart from the reflections from  $\gamma$  and  $\delta$ -ferrite. There are no  $\varepsilon$  martensite reflections present in this pattern. A detailed analysis of this pattern reveals that all of the higher intensity peaks belong to the  $\delta$ -ferrite phase and the intensity of the  $\gamma$  peaks are comparatively weaker, which indicates that the matrix phase, as shown in Figure 2(g), is  $\delta$ -ferrite. The weak reflections appearing from the  $\gamma$  phase are possibly due to the small volume fraction of large grains adjacent to the grain boundary intermetallic phase. Apart from the reflections coming from these two phases, all other reflections belong to the intermetallic phase, which appears along the grain boundary and inside the grains. A large number of possible intermetallic phases that form in this alloy system were considered to index this pattern. However, the best fit was obtained with  $\text{Fe}_5\text{Ni}_3\text{Si}_2$  intermetallic phase having a lattice parameter of 0.6137 nm and space group  $P2_13$ . So far no X-ray crystallographic data on this phase is available in the published literature, and the only X-ray crystallographic data available in the literature is on the  $\pi$  phase ( $\text{Cr}_3\text{Ni}_5\text{Si}_2$ ), which is isostructural with this phase<sup>[19]</sup> and normally observed in the Cr-Ni-Si alloy system. A further increase in Si to 10 pct leads to an increase in the amount of  $\text{Fe}_5\text{Ni}_3\text{Si}_2$  intermetallic phase and results in enhancement of the X-ray diffracted intensity of  $\text{Fe}_5\text{Ni}_3\text{Si}_2$  intermetallic phase, as shown in Figure 3(c). Surprisingly, in this pattern, no  $\gamma$  reflections are present, which indicates that the formation of  $\gamma$  phase does not take place beyond 8 pct Si. However, similar to alloy 8, in this alloy also, the matrix is  $\delta$ -ferrite.

The amounts of  $\varepsilon$  martensite present within the microstructure of these alloys (alloys 1 through 7) after water quenching from the solutionizing temperature were calculated by quantitative Rietveld phase analysis<sup>[20]</sup> using TOPAS software and are presented in Table II. The lattice parameters of these phases were



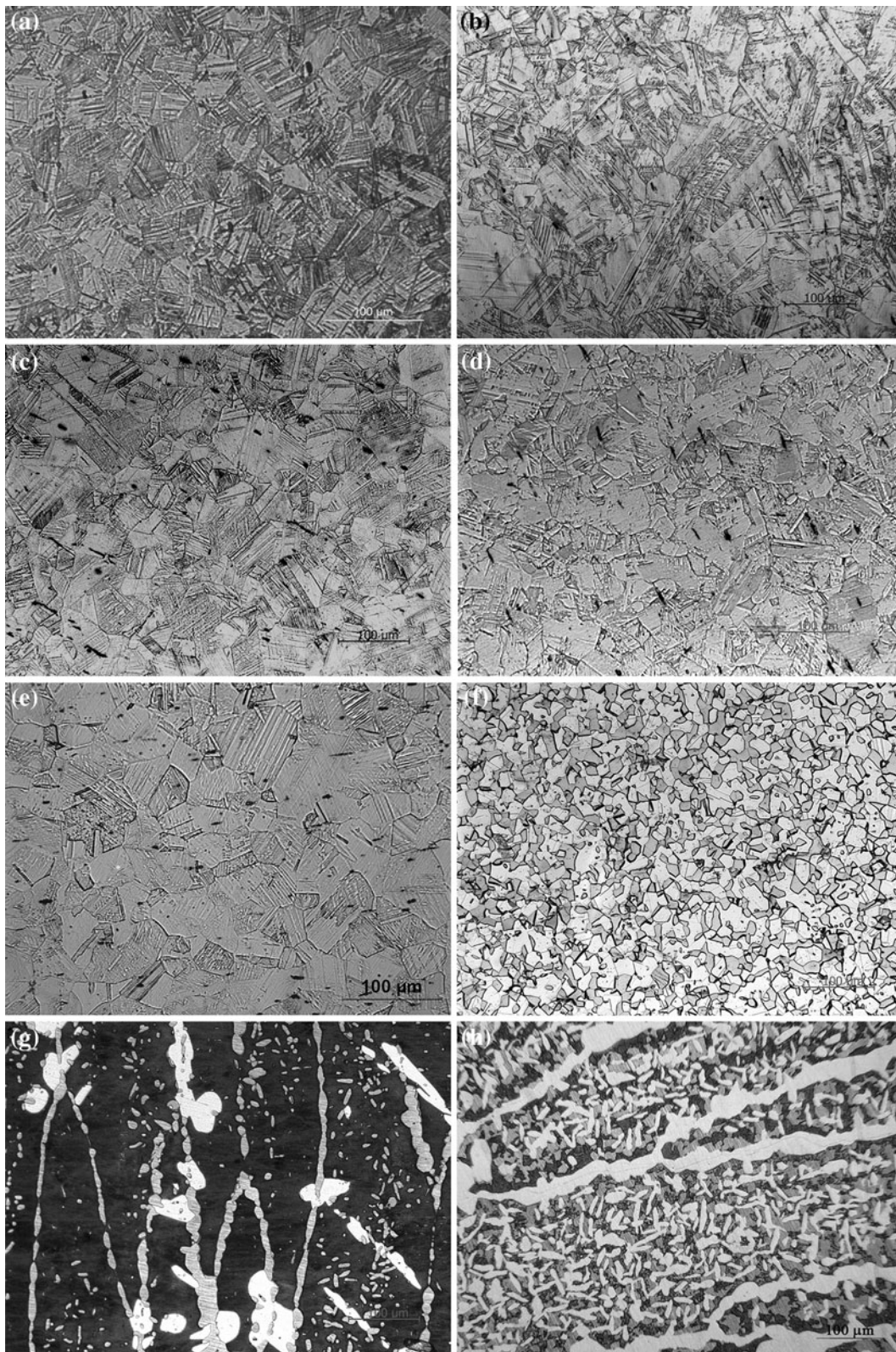


Fig. 2—Optical micrographs taken from solutionized specimens of (a) alloy 1, (b) alloy 3, (c) alloy 4, (d) alloy 5, and (e) alloy 6 showing the single-phase austenitic microstructure. Micrograph taken from (f) alloy 7 shows a two-phase microstructure of  $\gamma$  and  $\delta$ -ferrite. Optical micrographs of (g) alloy 8 and (h) alloy 10 showing the presence of  $\text{Fe}_5\text{Ni}_3\text{Si}_2$  type intermetallic phase along grain boundaries and inside grains.

also derived by whole pattern powder decomposition of the X-ray diffractograms using the Le Bail method.<sup>[21]</sup> The results obtained from the quantitative phase

analysis clearly show that with increasing Si amount the volume fraction of athermal  $\epsilon$  martensite decreases gradually.

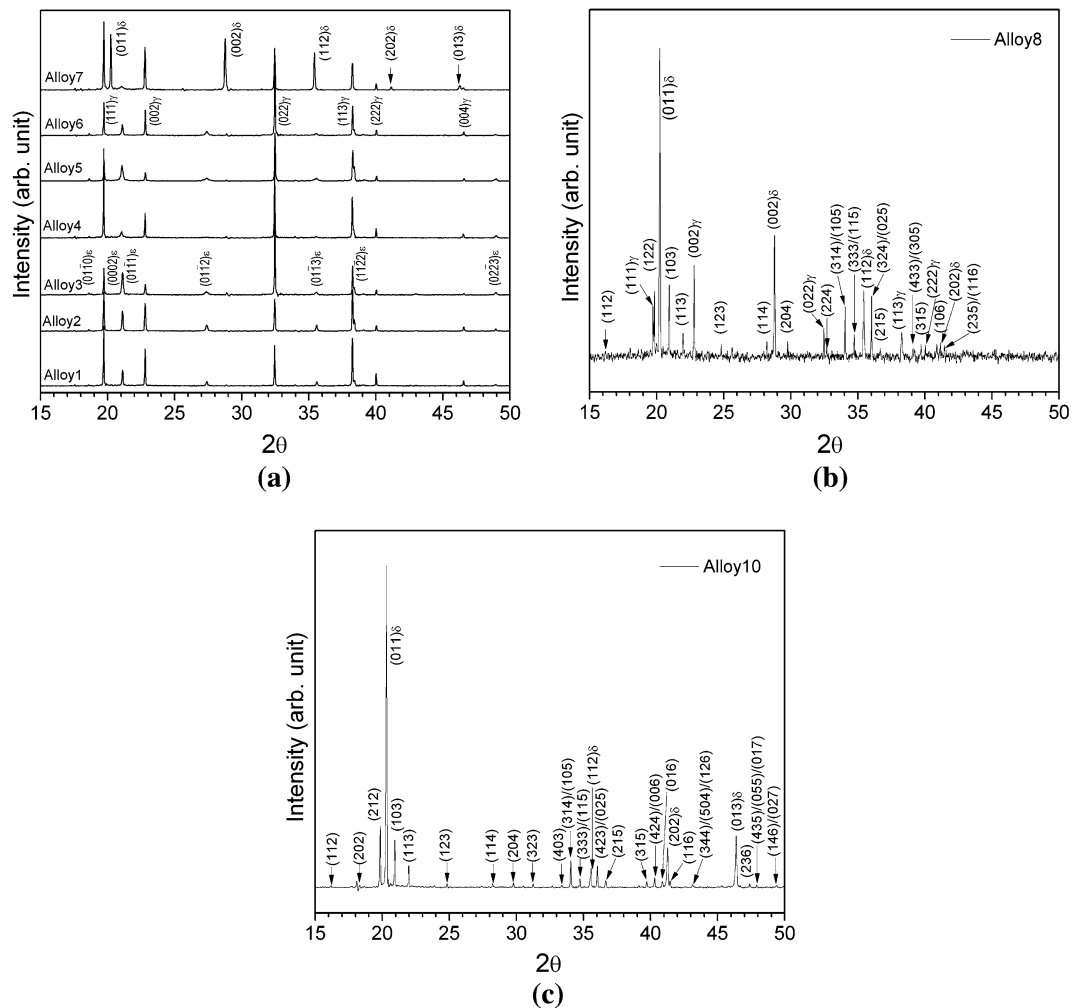


Fig. 3—XRD patterns of solutionized specimens: (a) alloys 1 through 7, (b) alloy 8, and (c) alloy 10 showing their phases constituents.

The chemical compositions of the phase constituents present in these alloys were determined using EPMA and given in Table III. As expected, the analysis clearly shows that in single-phase alloys (alloys 1 through 6) the composition of the  $\gamma$  phase agrees closely with the targeted alloy compositions. However, in the case of multiphase alloys (alloys 7 through 10), there is a redistribution of alloying elements between the phases. A comparison of the compositions of the  $\gamma$  and  $\delta$ -ferrite phases, as seen in alloy 7, shows that the matrix  $\gamma$  phase is richer in Ni and Mn and depleted in Cr and Si. Complementary to this, the  $\delta$ -ferrite phase gets richer in Cr and Si and leaner in Ni and Mn. These changes are expected because Ni and Mn are known to be austenite stabilizers and Cr and Si act as ferrite stabilizers.<sup>[18]</sup> In the case of alloy 8, the composition of the matrix phase, as compared to the phase that appears as bright large grains adjacent to the elongated grain boundary phase in Figure 2(g), is found to be richer in Cr and Si and lean in Ni and Mn. Therefore, the matrix phase in this alloy is definitely  $\delta$ -ferrite and the large grains are  $\gamma$  phase. This analysis also supports the observation made in the XRD pattern of this specimen, as mentioned previously. The composition analysis of the

plate-shaped  $\text{Fe}_5\text{Ni}_3\text{Si}_2$  intermetallic phase (as suggested by XRD) reveals that, unlike stoichiometric  $\text{Fe}_5\text{Ni}_3\text{Si}_2$  intermetallic phase, this phase contains all the alloying elements similar to the ferrite matrix or  $\gamma$  phase. However, this phase is enriched in Mn, Ni, Si, and Cr as compared to the other two phases present in the microstructure. The chemical composition of this phase in atomic percent is Fe-48.16, Cr-9.47, Ni-6.70, Mn-16.38, and Si-19.29. As revealed by the EPMA analysis, the atomic ratio of Fe, (Cr + Ni + Mn), and Si present in this phase is 48.16: 32.55: 19.29, respectively, which is almost close to the stoichiometric composition of the  $\text{Fe}_5\text{Ni}_3\text{Si}_2$  intermetallic phase. Therefore, it appears that this intermetallic phase is an off-stoichiometric  $\text{Fe}_5\text{Ni}_3\text{Si}_2$  intermetallic phase, in which the Ni site is shared by Ni, Mn, and Cr atoms. The composition analysis of the  $\text{Fe}_5\text{Ni}_3\text{Si}_2$  intermetallic phase in alloy 10 also shows a similar trend. The amounts of Fe, (Cr + Ni + Mn), and Si present in this specimen are 49.10, 30.75, and Si 20.15 at. pct, which are very close to the exact stoichiometric composition of  $\text{Fe}_5\text{Ni}_3\text{Si}_2$  phase.

Figure 4 shows the scanning electron micrographs taken from solutionized specimens of alloys 1, 7, 8, and 10. The micrograph of alloy 1 clearly reveals the



**Table II. Lattice Parameter and Quantitative Rietveld Phase Analysis**

			Volume Fraction (Pct)
Alloy	Phase	Lattice Parameters (nm)	
1	$\gamma$	$a = 0.359355$ nm	79
	$\varepsilon$	$a = 0.253890$ nm,	21
		$c = 0.410161$ nm	
2	$\gamma$	$a = 0.359263$ nm	65
	$\varepsilon$	$a = 0.2543903$ nm,	35
		$c = 0.410353$ nm	
3	$\gamma$	$a = 0.359234$ nm	62
	$\varepsilon$	$a = 0.253881$ nm,	38
		$c = 0.410851$ nm	
4	$\gamma$	$a = 0.359499$ nm	77
	$\varepsilon$	$a = 0.255803$ nm,	23
		$c = 0.405703$ nm	
5	$\gamma$	$a = 0.359205$ nm	79
	$\varepsilon$	$a = 0.254404$ nm,	21
		$c = 0.410272$ nm	
6	$\gamma$	$a = 0.359269$ nm	82
	$\varepsilon$	$a = 0.254098$ nm,	18
		$c = 0.410554$ nm	
7	$\gamma$	$a = 0.359225$ nm	44
	$\varepsilon$	$a = 0.252094$ nm,	7
		$c = 0.414406$ nm	
		$\delta$	$a = 0.285693$ nm

**Table III. Chemical Composition of Phases**

Alloy	Phase	Composition (Mass Pct)*			
		Cr	Ni	Mn	Si
1	$\gamma$	9.647	4.868	13.796	1.203
2	$\gamma$	9.540	4.819	13.450	2.268
3	$\gamma$	8.915	4.904	14.661	3.236
4	$\gamma$	9.591	4.900	14.040	4.762
5	$\gamma$	8.600	4.552	14.720	5.173
6	$\gamma$	8.700	4.732	14.352	5.929
7	$\gamma$	8.993	5.018	14.695	7.333
	$\delta$	10.278	4.425	13.372	8.480
8	$\delta$	9.442	4.590	13.711	9.561
	$\gamma$	8.290	5.288	15.407	7.839
10	$\text{Fe}_5\text{Ni}_3\text{Si}_2$	9.816	7.840	17.940	10.802
	$\delta$	8.929	3.668	11.903	11.005
	$\text{Fe}_5\text{Ni}_3\text{Si}_2$	10.473	6.831	16.389	11.350

\*Balance is Fe.

presence of  $\varepsilon$  martensite plates within the  $\gamma$  matrix. In the case of alloy 7 along with  $\gamma$  and blocky  $\delta$ -ferrite phase, as revealed under optical microscope, the  $\varepsilon$  martensite plates are also found to coexist within the  $\gamma$  phase. This observation supports the result obtained from XRD analysis. The  $\varepsilon$  martensite plates are seen to appear in all three possible orientations, which is a typical characteristic of self-accommodated athermal  $\varepsilon$  martensite.<sup>[22]</sup> Figure 4(c), the backscattered electron image taken from the alloy 8 specimen, shows a distinct Z contrast for three different phases in similitude to the optical micrographs shown in Figure 2(g). The  $\delta$ -ferrite

matrix appears dark; the  $\text{Fe}_5\text{Ni}_3\text{Si}_2$  intermetallic phase, which has platelike morphology, appears bright, and the  $\gamma$  grains that grow adjacent to the grain boundary appear gray. The difference in contrast of these phases can be easily justified by looking into the chemical composition of these phases. As mentioned in Table III, the  $\text{Fe}_5\text{Ni}_3\text{Si}_2$  intermetallic phase is richest in Mn, Ni, and Cr content as compared to the  $\gamma$  and  $\delta$ -ferrite matrix. Therefore, this phase appears as the brightest among these phases due to the higher yield of backscattered electrons from heavy elements such as Mn, Ni, and Cr. Between  $\gamma$  and  $\delta$ -ferrite, the former one contains slightly more Mn, Ni, and Fe than the  $\delta$ -ferrite matrix; thus, it appears a little brighter than the ferrite but darker than the  $\text{Fe}_5\text{Ni}_3\text{Si}_2$  intermetallic phase. The micrograph taken from alloy 10 (Figure 4(d)) shows some very interesting features when observed at higher magnification. It can be noticed that, apart from the presence of the  $\text{Fe}_5\text{Ni}_3\text{Si}_2$  intermetallic phase within the  $\delta$ -ferrite matrix, the ferrite phase appears in two different morphologies. Some of the grains are present in the form of blocky ferrite grains, and the rest have formed needle-shaped plates. As suggested by optical microscopy and XRD observation in this specimen, no  $\gamma$  phase was detected even under SEM.

### C. Transformation Temperatures

The transformation temperatures for the  $\gamma$ - $\varepsilon$  martensite transformation during cooling and reverse martensite to parent-phase transformation while heating were measured using DSC and are given in Table IV. The specimens used for this study were initially solution treated at 1273 K (1000 °C) and water quenched to room temperature. In order to avoid the influence of quenching stress on the transformation temperatures, these specimens were again heat treated at 873 K (600 °C) for 10 minutes and then slow cooled to room temperature. The DSC measurements were carried out in small specimens of around 40 to 50 mg weight in the temperature range of 198 K to 473 K (−75 °C to 200 °C). The results obtained from the DSC measurements, shown in Figure 5, clearly show that in these alloys Si addition up to 6 pct does not significantly change the austenite to martensite start transformation temperature ( $M_s$ ). However, there is a slight increase in martensite to austenite start transformation temperature ( $A_s$ ). Beyond 6 pct Si, the  $M_s$  and  $A_s$  temperatures are significantly lowered, and alloys containing more than 7 pct Si do not show any martensitic transformation. Interestingly, the enthalpy of  $\varepsilon$ - $\gamma$  transformation values obtained from these measurements decreases significantly with increasing Si amount. This indicates that the amount of athermal  $\varepsilon$  martensite in these alloys reduces with the increasing Si amount. These results also support our previous observations made under optical microscope and XRD analysis.

### D. Shape Recovery

Figure 6(b) displays the variation in shape recovery at different amounts of prestrain for alloys 1 through 7 in

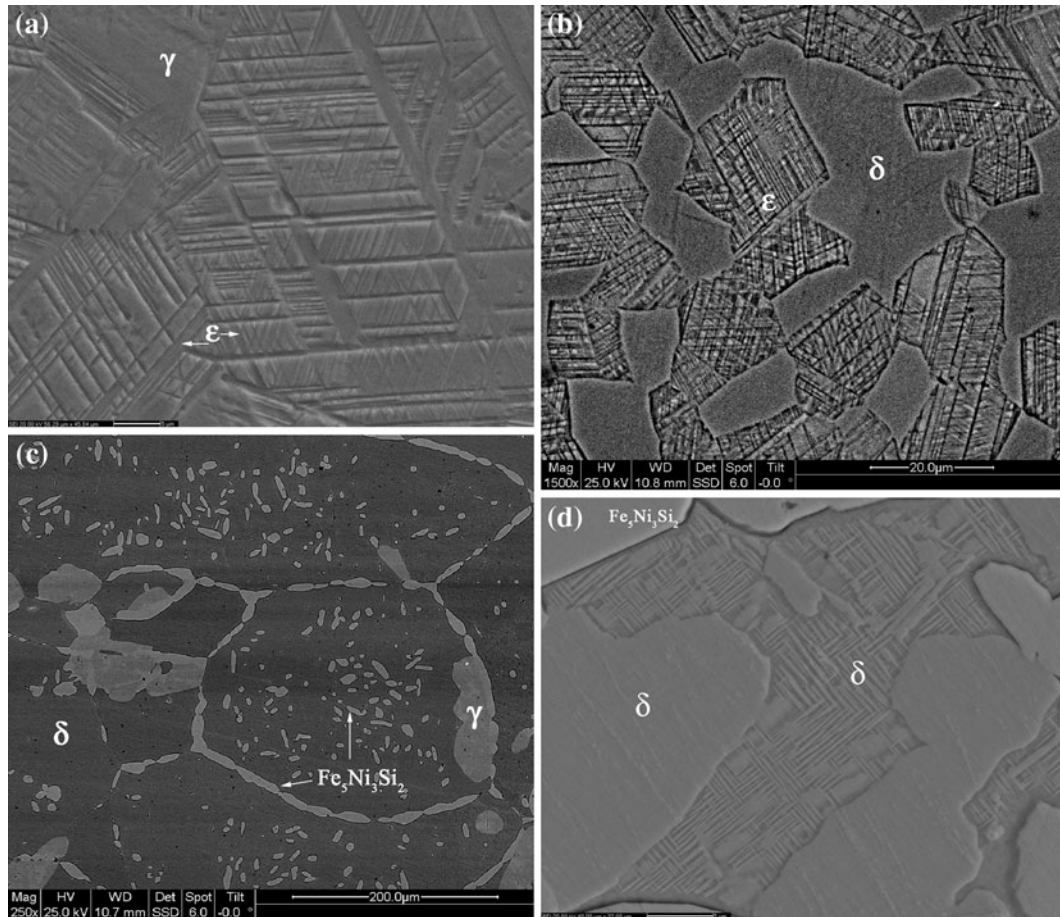


Fig. 4—Scanning electron micrographs showing (a)  $\epsilon$  martensite plates within  $\gamma$  matrix in alloy 1, (b)  $\delta$ -ferrite and  $\epsilon$  martensite within the  $\gamma$  phase in alloy 7, (c) plate-shaped  $\text{Fe}_5\text{Ni}_3\text{Si}_2$  type intermetallic plates and  $\gamma$  grains within the  $\delta$ -ferrite matrix in alloy 8, and (d)  $\text{Fe}_5\text{Ni}_3\text{Si}_2$  type intermetallic and  $\delta$ -ferrite in two different morphologies (blocky and acicular) in alloy 10.

**Table IV. Transformation Temperatures**

Alloy	$M_s$ (K)	$M_f$ (K)	$\Delta H$ ( $\gamma$ - $\epsilon$ ) (J/g)	$A_s$ (K)	$A_f$ (K)	$\Delta H$ ( $\epsilon$ - $\gamma$ ) (J/g)
1	304.96	251.13	4.20	375.88	416.28	3.72
2	303.11	267.56	5.83	385.89	414.03	4.68
3	296.59	260.99	4.21	387.17	413.73	3.37
4	308.23	280.75	3.32	396.87	416.17	3.07
5	308.88	281.89	2.15	401.63	421.81	2.16
6	298.58	272.14	0.96	395.51	417.72	1.31
7	243.19	230.19	0.24	358.46	385.15	0.33
8	—	—	—	—	—	—
10	—	—	—	—	—	—

solutionized condition. These plots essentially showed that in these alloys the amount of shape recovery increases monotonically with the increase in Si amount, except in the case of alloy 7. A detailed analysis of these plots revealed that, based on their shape recovery response, these alloys can be divided into two major classes: alloys containing up to 3 pct Si (alloys 1 through 3) show poor shape recovery (<60 pct at 4 pct prestrain) and alloys having Si between 4 and 6 pct (alloys 4 through 6) show good shape recovery (>60 pct at 4 pct prestrain). The highest amount of shape recovery was

observed in the case of alloy 6, and beyond that, the recovery starts deteriorating again. The lesser amount of shape recovery in the case of alloy 7 can be easily correlated to its microstructure. The microstructure of this alloy contains ~45 pct of  $\delta$ -ferrite; naturally, the amount of stress-induced  $\epsilon$  martensite formed in this alloy is less. The shape memory property of alloys 8 and 10 was not evaluated, because these alloys do not show any martensitic transformation.

### E. Mechanical Property

Figure 7(a) shows the stress-strain curves obtained from tensile tests carried out at room temperature using solutionized specimens of alloys 1 through 7. The room-temperature mechanical properties such as YS, ultimate tensile strength (UTS), and ductility values obtained from these tests are shown in Figure 7(b) and listed in Table V. The YS (0.2 pct proof stress) values, shown in Table V, are normally considered as the stress requirement to induce  $\epsilon$  martensite in these alloys. As observed from Figure 7(b), the YS of these alloys does not change substantially, at least up to 6 pct Si. This indicates that there is no significant increase in strength of  $\gamma$  matrix due to the increased amount of Si addition. Alloy 7

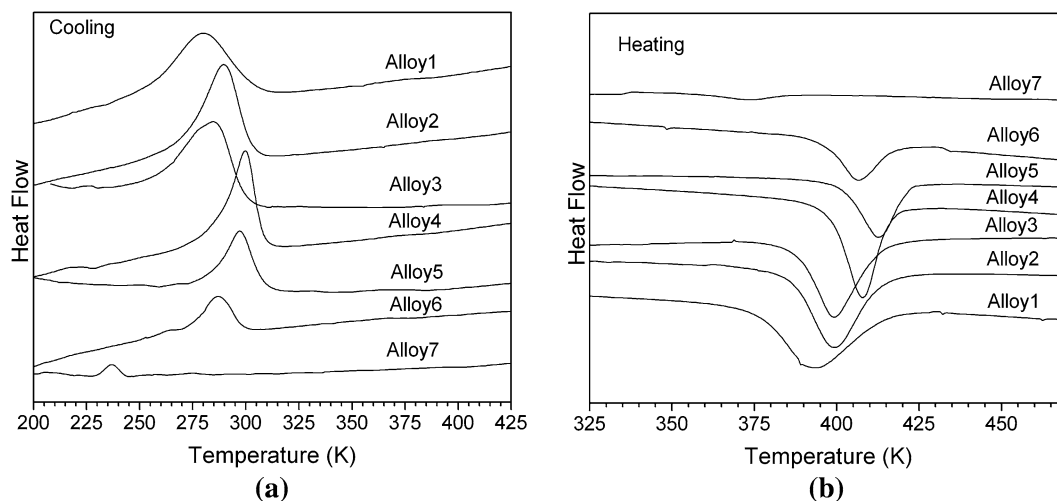


Fig. 5—Change in transformation temperatures due to Si addition: (a)  $\gamma$ - $\epsilon$  martensite forward transformation during cooling and (b)  $\epsilon$ - $\gamma$  reverse transformation during heating.

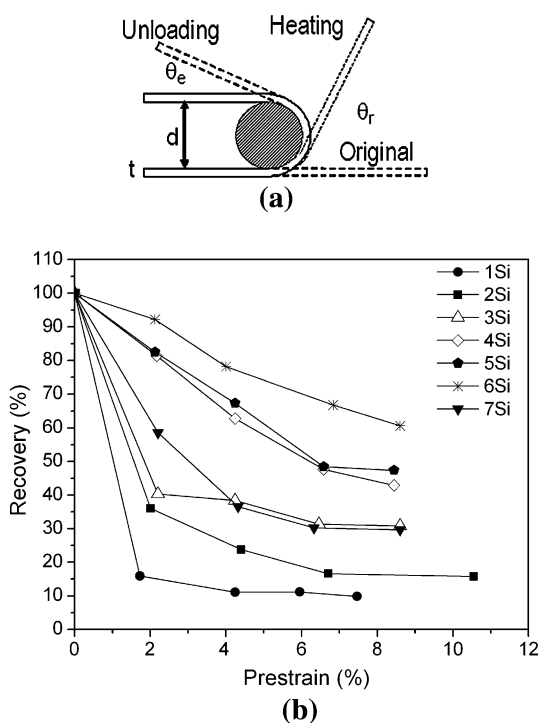


Fig. 6—(a) Schematic diagram of the bend test for measurement of shape recovery and (b) the improvement in shape recovery due to Si addition, measured in specimens solutionized at 1273 K (1000 °C) for 1 h.

shows the highest YS and lowest ductility, which is possibly due to the presence of a large volume of  $\delta$ -ferrite within the microstructure. The YS of alloy 3 is the lowest among the single-phase austenitic alloys, which may be a result of the greater amount of  $\epsilon$  martensite present (Table II) within its microstructure. The slight increase in YS in the case of alloy 5 could be due to its smaller grain size, as noticed in the optical micrograph shown in Figure 2(d).

The amount of ductility available in the case of alloy 7 becomes significantly less than the other six single-phase

austenitic alloys. In order to investigate the reason behind this, the fracture surface of the room-temperature tensile-tested specimens were observed under SEM and compared to alloy 6, which shows a very large amount of ductility. Figures 8(a) and (b) display the fractographs obtained from alloys 6 and 7, respectively. The fractograph obtained from alloy 6, which shows single-phase  $\gamma$  microstructure, clearly shows a typical ductile fracture with a large number of small size dimples. This is a clear indication of the cup and cone type fracture mode normally exhibited by highly ductile materials. Contrary to this, the fractograph taken from alloy 7 (Figure 8(b)) shows a typical cleavage type fracture, a characteristic usually shown by brittle materials. Apart from the flat faceted grains, some cracks could also be noticed in this specimen. These cracks possibly appear at the interface between the  $\gamma$  and  $\delta$ -ferrite due to the difference in the extent of deformation between these two phases. SEM observation of this fracture surface at still higher magnification reveals the presence of river markings within the faceted grains. Figure 8(c) shows such a fractograph, where these river markings are clearly seen within a grain. It appears that these grains are possibly  $\delta$ -ferrite grains, which have lower ductility.

#### F. Microstructure after Prestraining

The microstructural changes that take place after prestraining were investigated in solution-treated tensile specimens that were strained up to 5 pct at room temperature and unloaded to zero stress. The amount of stress-induced martensites formed after prestraining in these alloys (alloys 1 through 6) was estimated using X-ray diffractometry. The XRD patterns obtained from the gage length portion of these tensile specimens were used to determine the amounts of phase constituents using quantitative Rietveld analysis.<sup>[20]</sup> The X-ray diffractograms obtained from these alloys reveal that the  $\alpha'$  martensite reflections are absent in alloys with more than 3 pct Si. Figure 9 shows such diffractograms taken



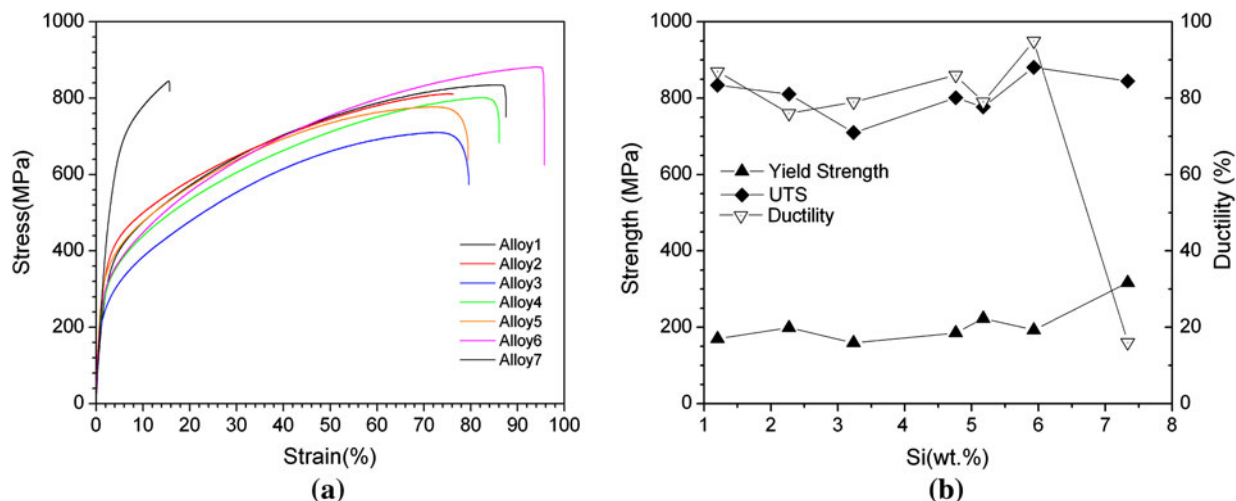


Fig. 7—(a) The stress-strain curves of solutionized specimens obtained from room-temperature tensile testing and (b) variation in room-temperature mechanical properties due to Si addition.

Table V. Room-Temperature Mechanical Properties

Alloy	YS (MPa)	UTS (MPa)	Ductility (Pct)
1	170	834	87
2	199	811	76
3	159	710	79
4	185	801	86
5	223	777	79
6	193	881	95
7	317	845	16

from prestrained specimens of alloys 1, 3, and 6, respectively. It is clearly evident from these diffractograms that, in the case of alloy 6, the  $\alpha'$  martensite peaks are not visible. This is possibly due to the fact that the amount of  $\alpha'$  martensite present in these alloys is less than the XRD detectable limit. The volume fractions of retained  $\gamma$  and stress-induced martensites ( $\epsilon$  as well as  $\alpha'$ ) calculated from these diffractograms are presented in Table VI. It was observed that the total amount of  $\epsilon$  martensite present within these microstructures after 5 pct prestraining remains almost the same in all alloys except in alloy 1. The highest amount of  $\epsilon$  martensite was obtained in the case of alloy 6. This could be the possible reason behind the maximum amount of shape recovery shown by this alloy.

Figures 10(a) and (b) are the optical and scanning electron micrographs taken from the alloy 2 specimen after 5 pct prestraining at room temperature. These micrographs essentially show that, although in most places stress-induced  $\epsilon$  martensites could be seen abundantly, in certain regions, the presence of stress-induced  $\alpha'$  martensite plates could also be noticed. These  $\alpha'$  martensites could be easily distinguished by their lenticular morphology from the usual stress-induced  $\epsilon$  martensite, which appears in the form of straight plates. The presence of these stress-induced  $\alpha'$  plates is mostly confined within bands of wide  $\epsilon$  martensite, which indicates that these  $\alpha'$  plates form through the  $\gamma$ - $\epsilon$ - $\alpha'$  transformation route during prestraining. This could be

the possible reason behind the low amount of recovery in alloys having Si less than 4 pct.

#### IV. DISCUSSION

The microstructural observations carried out in this study clearly showed that increasing amount of Si addition leads to the formation of many new phases in these alloys. The microstructural characterization of the 1273 K (1000 °C) solution-heat-treated specimens revealed that in these alloys the microstructure remains single-phase  $\gamma$  up to 6 pct Si addition. However, alloys with more than 6 pct Si show a microstructure composed of  $\gamma$  +  $\delta$ -ferrite phase. Generally, the formation of  $\delta$ -ferrite phase has been noticed in these alloys after heat treatment at higher temperature.<sup>[23]</sup> The presence of  $\text{Fe}_5\text{Ni}_3\text{Si}_2$  type intermetallic phase has been noticed in alloys containing more than 7 pct Si. Therefore, it looks like the stability of the  $\gamma$  phase decreases when the microstructure contains more than 6 pct Si. The appearance of  $\delta$ -ferrite phase in alloys containing more than 6 pct Si is related to the higher amount of Si addition, which is a well-known ferrite stabilizer.<sup>[18]</sup> The addition of a higher amount of Si possibly extends the stability of the  $\delta$ -ferrite phase toward the lower temperature. This effect becomes more prominent when the amount of Si becomes more than 8 pct. As could be noticed, in the alloy containing 10 pct Si, the  $\gamma$  phase is totally absent within the microstructure. The formation of  $\delta$ -ferrite and  $\text{Fe}_5\text{Ni}_3\text{Si}_2$  type intermetallic phase was reported earlier by Maji *et al.*<sup>[23]</sup> in the Fe-Mn-Si-Cr-Ni alloy. However, the  $\text{Fe}_5\text{Ni}_3\text{Si}_2$  type intermetallic phase only precipitates out after aging in the temperature range of 973 K to 1173 K (700 °C to 900 °C) at the tri junctions of grain boundaries. The amount of this intermetallic phase was very little and the temperature range where this precipitation occurs was also lower than the solution treatment temperature used in this study. The emergence of  $\delta$ -ferrite in two different morphologies in the case of alloy 10 can be explained as follows: this

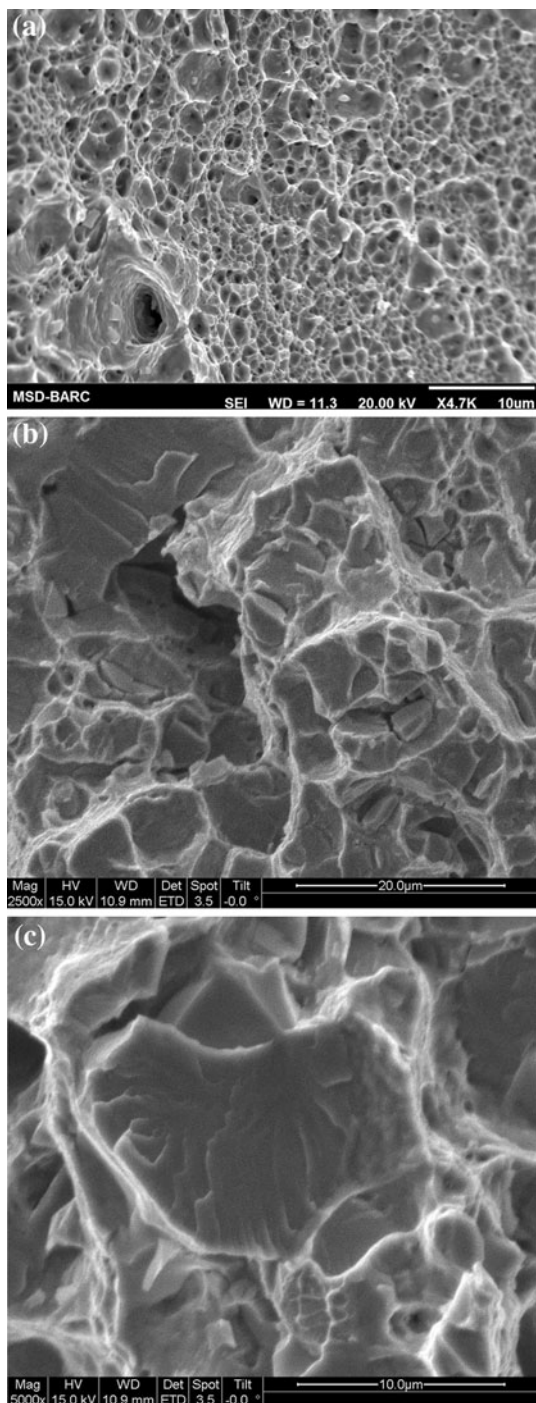


Fig. 8—Scanning electron micrographs taken from the fracture surface of (a) alloy 6 and (b) and (c) alloy 7 showing the difference in fracture mode during room-temperature tensile deformation.

alloy was possibly heat treated in the two-phase field of  $\gamma + \delta$ -ferrite while solution annealing. The primary  $\delta$ -ferrite grains present at that temperature remain as blocky ferrite grains, while the  $\gamma$  grains transform to acicular ferrite during the process of water quenching.

The improvement of shape recovery with increasing amounts of Si addition observed in these alloys can be justified by looking into their microstructural details

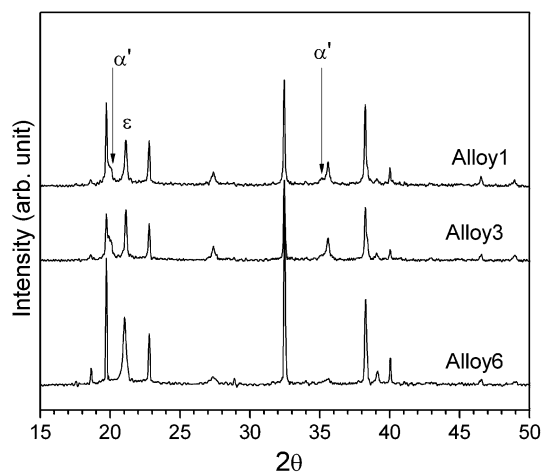


Fig. 9—XRD patterns obtained from alloys 1, 3, and 6 after 5 pct prestraining at room temperature showing the presence of stress-induced  $\alpha'$  martensite in alloys containing less than 4 pct Si.

**Table IV. Volume Fraction of Parent and Martensite Phases after Prestraining**

Alloy	Volume Fraction of Phases (Pct)		
	$\gamma$	$\varepsilon$	$\alpha'$
1	54	33	13
2	43	47	10
3	45	44	11
4	53	47	—
5	56	44	—
6	52	48	—

after prestraining. The XRD patterns obtained from the prestrained specimens give an idea about the total amount of  $\varepsilon$  martensite present within the microstructure after prestraining. Figure 11 shows the change in volume fraction of athermal, total, and stress-induced  $\varepsilon$  martensites with Si addition. The amount of stress-induced  $\varepsilon$  martensite formed due to prestraining is the difference between the total amount of  $\varepsilon$  martensite present within the microstructure after 5 pct prestraining and the athermal  $\varepsilon$  martensite present after solutionization before prestraining. It could be noticed that the total amount of  $\varepsilon$  martensite present within these microstructures after 5 pct prestraining remains almost the same in all alloys except in alloy 1. On the other hand, the amount of athermal  $\varepsilon$  martensite present before prestraining was seen to decrease with the Si amount. Naturally, the amount of  $\varepsilon$  martensite formed due to prestraining will increase with increasing Si addition. The amount of stress-induced  $\varepsilon$  martensite remains low up to 3 pct Si; after that, it steadily increases up to 6Si. The highest amount of stress-induced  $\varepsilon$  martensite was obtained in the case of alloy 6, which shows the best shape recovery also. Therefore, it looks like that the amount of recovery is proportional to the amount of stress-induced  $\varepsilon$  martensite. The amount of stress-induced  $\alpha'$  martensite, which acts as a barrier

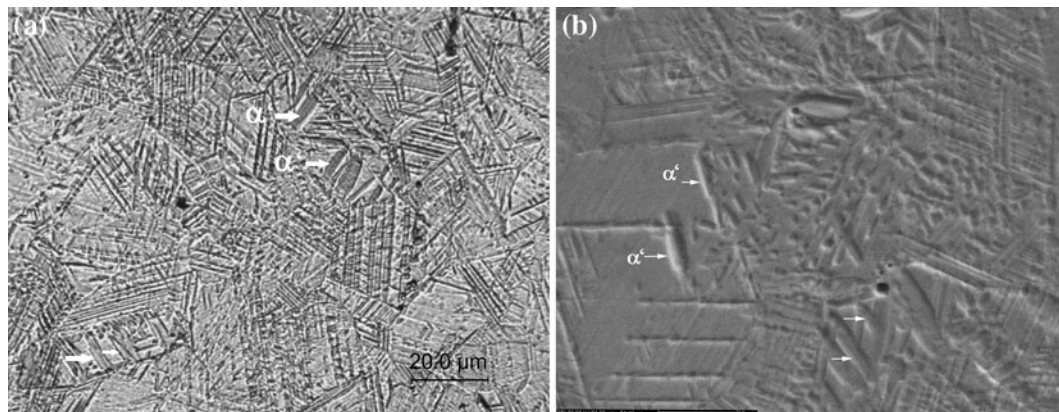


Fig. 10—(a) Optical and (b) scanning electron micrographs taken from alloy 2 after 5 pct prestraining showing the presence of stress-induced  $\alpha'$  martensite formed through  $\gamma$ - $\varepsilon$ - $\alpha'$  transformations.

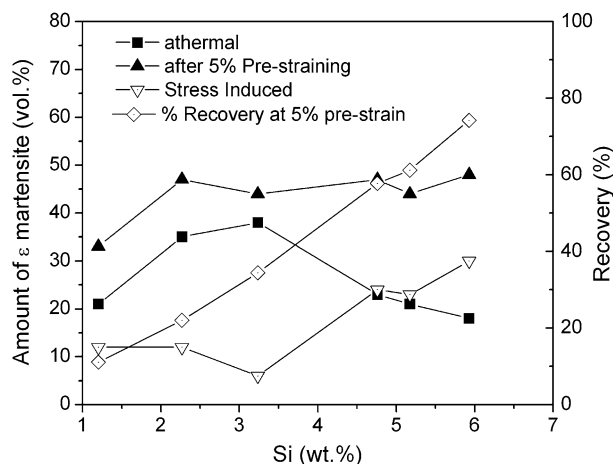


Fig. 11—Effect of Si addition on the volume fraction of athermal and stress-induced  $\varepsilon$  martensite and its consequence on shape recovery.

toward the motion of the Shockley partial dislocations during reverse transformation, could be easily detected by powder XRD in alloys having Si up to 3 pct (Figure 9). Beyond this, only stress-induced  $\varepsilon$  martensite has been observed. Thus, most likely in alloys with Si > 3 pct stress-induced  $\gamma$ - $\varepsilon$ - $\alpha'$  transformation does not take place, or if at all, the amount of  $\alpha'$  martensite formed is less than the detectable limit of the powder XRD. Microstructural observation of these alloys under optical microscope also does not show any such stress-induced  $\alpha'$  martensite after prestraining. Therefore, it is apparent that the poor shape recovery associated with alloys having less than 4 pct Si is primarily due to this stress-induced  $\gamma$ - $\varepsilon$ - $\alpha'$  transformation.

Federzoni and Guenin<sup>[24]</sup> illustrated that the formation of stress-induced  $\varepsilon$  martensite is insensitive to the presence of athermal  $\varepsilon$  martensite when the amount of prestrain is less than 3 pct. However, under large deformation, the presence of pre-existing athermal  $\varepsilon$  martensite acts as a barrier to the formation of new stress-induced  $\varepsilon$  martensite. Jun *et al.*<sup>[25]</sup> reported that, if there is a minor amount of pre-existing athermal

$\varepsilon$  martensite, further prestraining leads to the continuous formation of  $\varepsilon$  martensite from the parent  $\gamma$  phase. On the other hand, the presence of a higher amount of pre-existing athermal  $\varepsilon$  martensite leads to the coalescence of the exiting  $\varepsilon$  martensite through a reorientation process during prestraining, and usually the formation of  $\alpha'$  martensite takes place due to the interaction of two intersecting variants of  $\varepsilon$  martensite at the intersection of these plates. This  $\alpha'$  martensite is normally referred to as “window type”  $\alpha'$  martensite<sup>[26,27]</sup> and acts as an effective barrier during the reversible motion of the Shockley partial dislocations responsible for the shape recovery in these alloys.

The deterioration of shape recovery in alloys with more than 4 pct Si at higher amount of prestrain is possibly limited by the formation of strain-induced window type  $\alpha'$  martensite. The volume fraction of this strain-induced  $\alpha'$  martensite is usually much lower and could not be detected by powder XRD. Similar results already exist in the published literature,<sup>[26,27]</sup> in support of this phenomenon. As indicated earlier, the poor recovery associated with alloys having Si less than 4 pct is mostly due to the stress-induced  $\gamma$ - $\varepsilon$ - $\alpha'$  transformation, which adds to the irrecoverable part of the prestrain. However, a closer look into the percent recovery vs amount of Si curve presented in Figure 11 reveals that, irrespective of the formation of stress-induced  $\alpha'$  martensite, the recovery tends to increase with Si addition. This could possibly happen if the pre-existing athermal  $\varepsilon$  martensite, which was present before prestraining, reoriented itself pseudoplastically and contributed to the shape recovery. However, the contribution from pseudoplastic reorientations of athermal  $\varepsilon$  martensite may be very limited in alloys with higher Si content, as the volume fraction of athermal  $\varepsilon$  martensite was comparatively low. Now, the question remains unanswered whether the stress-induced  $\alpha'$  martensite has any contribution to the shape recovery of these alloys. Zhao<sup>[28]</sup> showed that the presence of  $\alpha'$  martensite within the microstructure can improve the shape recovery. He pointed out that the elastic energy stored within the  $\alpha'$  martensite while prestraining can decrease the reverse transformation temperature and result in a smaller



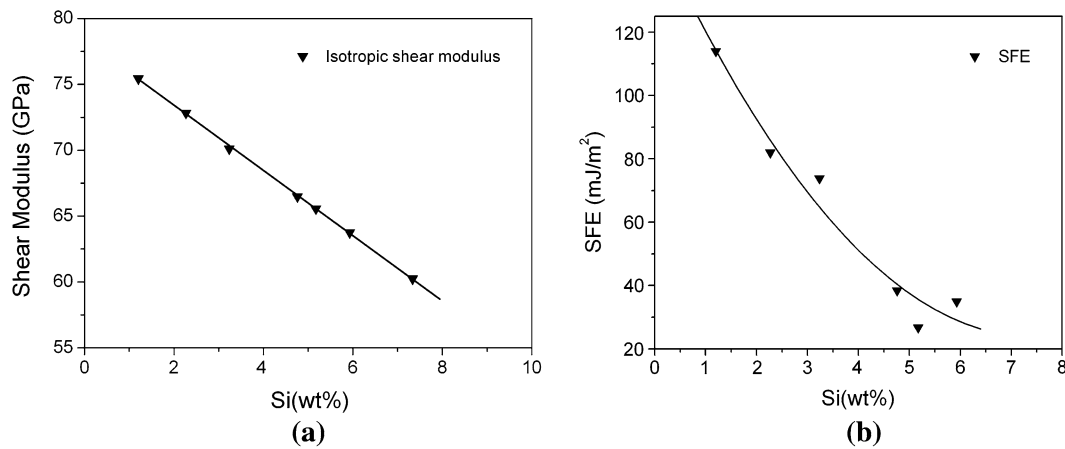


Fig. 12—Change in (a) shear modulus and (b) SFE due to Si addition.

driving force for reverse transformation. In other words, the relaxation of this elastically stored energy during reverse transformation can lead to improved shape recovery, because this energy will help in overcoming the energy barrier required for the reverse motion of the Shockley partial dislocations, which is responsible for the shape recovery observed in these alloys. However, further experiments are required to elucidate this point.

The formation of a higher amount of stress-induced  $\varepsilon$  martensite with an increase in Si addition could be correlated with the SFE of these alloys. The SFE of these alloys was estimated by measuring the probability of the stacking fault from the X-ray line profile analysis of these single-phase austenitic alloys (alloys 1 through 6) using the Warren–Averbach technique.<sup>[29]</sup> The SFE was calculated from the stacking fault probability values using the relationship proposed by Schramm and Reed.<sup>[30]</sup> In order to calculate the SFE using their formulation, it is necessary to know the shear modulus along the (111) plane, which is normally measured on single crystal. However, thus far, nobody has reported these values for Fe-Mn-Si-Cr-Ni alloys. In the absence of these data in the literature, it was assumed that the shear modulus of these alloys is isotropic and may be replaced with the macroscopic shear modulus ( $G$ ). The macroscopic shear modulus ( $G$ ) for the  $\gamma$  phase was calculated using the formulation given by Ghosh and Olson.<sup>[31]</sup> The macroscopic shear modulus of these alloys was observed to decrease monotonically with Si addition and is shown in Figure 12(a). Figure 12(b) shows the change in SFE of these alloys with increasing Si amount. As observed, the SFE of these alloys decreases with the higher amount of Si addition. Therefore, it appears that, with the decrease in SFE and shear modulus in these alloys, stress inducing  $\varepsilon$  martensite becomes easier with the higher amount of Si. The room-temperature YS (0.2 pct proof stress), which is usually taken as an indicator for the stress requirement to induce  $\varepsilon$  martensite in these alloys, did not show any significant decrease with the higher amount of Si addition. Therefore, it appears that this room-temperature

YS is more closely related to the mechanical strength of these alloys.

It is surprising that the amount of athermal  $\varepsilon$  martensite decreases with the higher amount of Si addition, when it should have increased due to the decrease in SFE of these alloys. This apparent contradiction suggests the possibility that, most likely, the nucleation of  $\varepsilon$  martensite is affected by Si addition. The amount of pre-existing nuclei available in these alloys is possibly limited and further deteriorates with the higher amount of Si addition. Therefore, the amount of athermal  $\varepsilon$  martensite becomes less with the increasing amount of Si addition. The volume fraction of stress-induced  $\varepsilon$  martensite increases with Si; this could possibly happen if the generation of nuclei takes place by concomitant plastic deformation during straining of the  $\gamma$  phase; *i.e.*, the yield stress of these alloys could be close to the critical stress to induce martensite. An indirect evidence of this insufficiency of pre-existing nuclei can also be seen from the results obtained after thermal cycling of these alloys. Tsuzaki *et al.*<sup>[14]</sup> noticed that in Fe-24Mn-6Si alloy the amount of  $\varepsilon$  martensite increases from less than 30 to 40 pct just by 10 thermal cyclings below  $M_s$  (305 K (32 °C)) and above  $A_f$  (573 K (300 °C)). However, the similar effect was not seen when the same alloy was thermally cycled between 305 K and 873 K (32 °C and 600 °C). This is possibly related to the amount of pre-existing nuclei available within the material for athermal  $\varepsilon$  martensite formation. As the availability of pre-existing nuclei increases, the amount of  $\varepsilon$  martensite also becomes higher and *vice versa*.

This study showed that at least 4 pct Si is necessary to avoid stress-induced  $\gamma$ - $\varepsilon$ - $\alpha'$  transformation, and the addition of more than 6 pct Si is not beneficial due to the formation of  $\delta$ -ferrite. This study also revealed that Si addition up to 6 pct does not affect the transformation temperature and the mechanical properties of  $\gamma$  phase, though it reduces the formation of athermal  $\varepsilon$  martensite and also the SFE. On the other hand, this study showed that good shape recovery is observed when the transformation temperature is close to room

temperature, when there is only little pre-existing athermal  $\varepsilon$  martensite, when the SFE is low, and when the yield stress of the matrix is close to the critical stress to induce  $\varepsilon$  martensite. It is in this context that the role of Si in improving the shape recovery becomes apparent.

## V. CONCLUSIONS

The important results obtained from this study can be summarized as follows.

1. In FeMnSiCrNi alloys, the microstructure remains single-phase  $\gamma$  up to 6 pct Si addition only. Alloys containing more than 6 pct Si show a microstructure composed of  $\gamma + \delta$  ferrite phases. The  $\text{Fe}_5\text{Ni}_3\text{Si}_2$  type intermetallic phase starts appearing in the microstructure beyond 7 pct Si addition.
2. Alloys containing more than 7 pct Si cannot be hot rolled due to the presence of brittle  $\text{Fe}_5\text{Ni}_3\text{Si}_2$  type intermetallic phase.
3. Silicon addition does not affect the transformation temperature and mechanical properties of the  $\gamma$  phase until 6 pct, though the amount of shape recovery is observed to increase monotonically.
4. The SME observed in these alloys is essentially due to the stress-induced  $\varepsilon$  martensite. The extent of shape recovery is proportional to the amount of stress-induced  $\varepsilon$  martensite formed during prestraining. The observation of poor shape recovery in alloys with Si less than 4 pct and more than 6 pct is due to the formation of stress-induced  $\alpha'$  martensite through  $\gamma$ - $\varepsilon$ - $\alpha'$  transformation and the large volume fraction of  $\delta$ -ferrite, respectively.
5. Silicon addition appears to decrease the SFE of FeMnSiCrNi alloys.

## ACKNOWLEDGMENTS

The authors are grateful to Dr. A.K. Suri, Director, Materials Group, BARC, and Dr. G.K. Dey, Head, Materials Science Division, BARC, for their support and encouragement for the work on shape memory alloys. We thank Mr. A. Laik, Dr. C.B. Basak, and Dr. S. Majumdar for the help received in carrying out the EPMA and SEM during this work. We are also grateful to Messrs. V.C. Krishnamohan Nair and S. Yadav for the melting and fabrication of alloys used in this work.

## REFERENCES

1. K. Enami, A. Nagasawa, and S. Nenno: *Scripta Metall.*, 1975, vol. 9, pp. 941–48.
2. A. Sato, E. Chisima, K. Soma, and T. Mori: *Acta Metall.*, 1982, vol. 30, pp. 1177–83.
3. M. Murakami, H. Otsuka, H. Suzuki, and S. Matsuda: *Trans. ISIJ*, 1987, vol. 27, p. B-88.
4. H. Otsuka, H. Yamada, H. Tanahashi, and T. Maruyama: *Mater. Sci. Forum*, 1990, vols. 56–58, pp. 655–60.
5. T.Y. Hsu: *J. Mater. Sci. Technol.*, 1994, vol. 10, pp. 107–10.
6. A. Ariapour, I. Yakubtsov, and D. Perovic: *Metall. Mater. Trans. A*, 2001, vol. 32A, pp. 1621–28.
7. H. Otsuka, S. Kajiwarra, and T. Ishihara: *Mater. Charact.*, 1994, vol. 32, pp. 229–35.
8. S. Kajiwarra, D. Liu, T. Kikuchi, and N. Shinya: *Scripta Mater.*, 2001, vol. 44, pp. 2809–14.
9. A. Sato, Y. Yamaji, and T. Mori: *Acta Metall.*, 1986, vol. 34, pp. 287–94.
10. M. Murakami, H. Otsuka, H. Suzuki, and S. Matsuda: *Proc. Int. Conf. on Martensitic Transformations (ICOMAT-86)*, Nara, Japan, 1986, pp. 985–90.
11. M. Andersson, R. Stalmans, and J. Agren: *Acta Metall.*, 1998, vol. 46, pp. 3883–91.
12. A.A. Gulyaev: *J. Phys. IV*, 1995, vol. 5, pp. 469–74.
13. X. Tian and Y. Zhang: *Mater. Sci. Eng. A*, 2009, vol. 516A, pp. 73–77.
14. K. Tsuzaki, M. Ikegami, Y. Tomota, K. Kurokawa, W. Nakagawara, and T. Maki: *Mater. Trans. JIM*, 1992, vol. 33, pp. 236–70.
15. Y. Tamota, M. Piao, T. Hasunuma, and Y. Kimura: *Jpn. Inst. Met.*, 1990, vol. 54, pp. 628–34.
16. V.G. Gavriljuk, V.V. Bliznuk, B.D. Shanina, and S.P. Kolesnik: *Mater. Sci. Eng. A*, 2005, vol. 406A, pp. 1–10.
17. H. Otsuka, H. Yamada, T. Maruyama, H. Tanahashi, S. Matsuda, and M. Murakami: *ISIJ Int.*, 1990, vol. 30, pp. 674–79.
18. F.B. Pickering: *Physical Metallurgy and the Design of Steels*, Applied Science Publishers Ltd, London, 1978, p. 226.
19. E.I. Gladyshevskii, P.I. Kripyakevich, and Y.B. Kuz'ma: *J. Str. Chem.*, 1962, vol. 3, pp. 402–10.
20. H.M. Rietveld: *Acta Cryst.*, 1967, vol. 22, pp. 151–52.
21. A. Le Bail, H. Duroy, and J.L. Fourquet: *Mater. Res. Bull.*, 1988, vol. 23, pp. 447–52.
22. J.H. Yang and C.M. Wayman: *Mater. Character.*, 1992, vol. 28, pp. 23–35.
23. B.C. Maji, M. Krishnan, and V.V. Rama Rao: *Metall. Mater. Trans. A*, 2003, vol. 34A, pp. 1029–42.
24. L. Federzoni and G. Guenin: *Scripta Metall. Mater.*, 1994, vol. 31, pp. 25–30.
25. J.H. Jun, W. Jin, and C.S. Choi: *Scripta Metall. Mater.*, 1995, vol. 33, pp. 1339–44.
26. J.H. Yang and C.M. Wayman: *Metall. Trans. A*, 1992, vol. 23A, pp. 1445–54.
27. B.C. Maji and M. Krishnan: *Scripta Mater.*, 2003, vol. 48, pp. 71–77.
28. C. Zhao: *Metall. Mater. Trans. A*, 1999, vol. 30A, pp. 2599–2604.
29. B.E. Warren and B.L. Averbach: *J. Appl. Phys.*, 1950, vol. 21, pp. 595–99.
30. Schramm and R.P. Reed: *Metall. Trans. A*, 1975, vol. 6A, pp. 1345–51.
31. G. Ghosh and G.B. Olson: *Acta Mater.*, 2002, vol. 50, pp. 2655–75.